

A Linearized $k - \epsilon$ Model of Forest Canopies and Clearings

Antonio Segalini¹ · Tetsuya Nakamura² · Koji Fukagata²

Received: 7 September 2015 / Accepted: 7 July 2016 / Published online: 18 July 2016
© The Author(s) 2016. This article is published with open access at Springerlink.com

Abstract A linearized analysis of the Reynolds-averaged Navier–Stokes (RANS) equations is proposed where the $k - \epsilon$ turbulence model is used. The flow near the forest is obtained as the superposition of the undisturbed incoming boundary layer plus a velocity perturbation due to the forest presence, similar to the approach proposed by Belcher et al. (J Fluid Mech 488:369–398, 2003). The linearized model has been compared against several non-linear RANS simulations with many leaf-area index values and large-eddy simulations using two different values of leaf-area index. All the simulations have been performed for a homogeneous forest and for four different clearing configurations. Despite the model approximations, the mean velocity and the Reynolds stress $\overline{u'w'}$ have been reasonably reproduced by the first-order model, providing insight about how the clearing perturbs the boundary layer over forested areas. However, significant departures from the linear predictions are observed in the turbulent kinetic energy and velocity variances. A second-order correction, which partly accounts for some non-linearities, is therefore proposed to improve the estimate of the turbulent kinetic energy and velocity variances. The results suggest that only a region close to the canopy top is significantly affected by the forest drag and dominated by the non-linearities, while above three canopy heights from the ground only small effects are visible and both the linearized model and the simulations have the same trends there.

Keywords Canopy flows · Forest clearings · Linearized Reynolds-averaged Navier–Stokes equations

1 Introduction

The study of the atmospheric boundary layer over forested areas has numerous applications in micrometeorology and wind energy but, despite much effort, there are still numerous

✉ Antonio Segalini
segalini@mech.kth.se

¹ Linné FLOW Centre, KTH Mechanics, 100-44 Stockholm, Sweden

² Department of Mechanical Engineering, Keio University, Yokohama, Japan

open questions, especially regarding complex terrain and how complex forest configurations modify the flow field above and in the wake of forests. Intensive research efforts have focussed on describing the flow field over a homogeneous forest canopy (Stacey et al. 1994; Irvine et al. 1997; Harman and Finnigan 2007; Segalini et al. 2013; Arnqvist et al. 2015), where it is assumed that the streamwise extension of the canopy is at least one order of magnitude larger than the local boundary-layer thickness, δ . Under this condition, it can be expected that the canopy flow achieves an equilibrium state within the internal canopy boundary layer (Garratt 1990) both above and below the canopy top, located at $z = h_c$. Most numerical simulations and analytical analyses have been performed within a homogeneous framework, which allows significant simplification of the equations since the streamwise gradients vanish. In typical forests, however, this condition is never fulfilled because forested areas are not infinitely long and they have boundaries. Furthermore, forests can be inhomogeneous in many parameters, such as the local tree height, foliage characteristics and leaf-area density. If there is a significant area (of size comparable to the tree height) where trees are absent, it is generally referred to as a *clearing*.

The first complication one encounters is due to the finite boundaries of the forest, where most of the current idealized models are not valid due to the presence of a narrow transition region (of the order of a few canopy heights) near the forest edges. Here the flow properties tend to deviate between two different equilibrium states. Recently, large-eddy simulations (LES) have become reliable and provide additional evidence (Yang et al. 2006; Dupont and Brunet 2009; Silva Lopes et al. 2013) in the quest to understand the flow over complex forest configurations. However, LES is computationally expensive while, on the other hand, experiments require dedicated facilities and have limitations regarding the specification of boundary conditions (such as initial conditions, leaf-area density, etc.) that prohibit a full characterization. One alternative to LES is provided by Reynolds-averaged Navier–Stokes (RANS) simulations that aim at the characterization of the mean flow properties and Reynolds stress, significantly reducing the computational cost with respect to LES. On the other hand, the quality of RANS simulations heavily depends on the turbulence closure model employed, and different hierarchies of models with different complexities exist (Mellor and Yamada 1982; Hanjalic 2005; Zilitinkevich et al. 2013). The problem is further complicated over forests since the forest applies a significant drag to the incoming flow, providing a spectral shortcut in the energy transfer between large and small scales of motion (Baldocchi and Hutchison 1988; Finnigan 2000). Svensson and Häggkvist (1990) and Katul et al. (2004) suggested modifying the standard $k - \epsilon$ model equations for k and ϵ (namely the turbulent kinetic energy and the rate of turbulent kinetic energy dissipation, respectively) to account for such mechanisms. Silva Lopes et al. (2013) provided expressions for the additional terms in the $k - \epsilon$ equations, validating them for several flow cases with different complexities.

Currently, few analytical solutions are able to account for the presence of clearings. Belcher et al. (2003), for instance, proposed a model based on linearized two-dimensional RANS equations, where the boundary-layer approximation was enforced by neglecting the turbulent streamwise momentum diffusion and a mixing-length model was used to represent the shear stress as $-\overline{u'w'} = l_m^2 (dU/dz)^2$, in which $l_m(z)$ is the mixing length and dU/dz is the streamwise velocity gradient in the vertical direction. By assuming that l_m increases linearly with height, the authors were able to analytically solve the first-order problem and to estimate consequently the mean velocity field. However, as the authors noted, the mixing length can be affected by the canopy presence (for instance through a vertical shift of the l_m profile, see Sogachev and Kelly 2015), so that the model suffered from ambiguity in the choice of the mixing length and of the lack of an adjustment region for it. A complete model, such as a two-equation model, overcomes this difficulty with the cost that additional

equations must be solved. Linearized methods significantly reduce the complexity of the equations and are amenable to the use of the Fourier transform in the horizontal plane, so that high numerical accuracy is achieved but with a reduced computational effort (Shen et al. 2011). With the aim of performing a large number of simulations for an empirical characterization of a generic forest, linearized methods are indeed very appealing. The present paper is therefore aimed at the development of a linearized RANS solution with the modified $k - \epsilon$ model proposed by Silva Lopes et al. (2013). In Sect. 2 the derivation of the model equations is provided, together with a full account of the numerical solver used. In order to validate the model, LES was performed with different clearing configurations and different forest densities, as discussed in Sect. 3. The quantification of the linearization error is reported in Sect. 4 where the comparison between linear and non-linear RANS is discussed. The results of the validation efforts are shown in Sect. 5 while Sect. 6 offers concluding remarks.

2 Mathematical Model

Let us consider a boundary layer, with mean streamwise velocity component $U_0(z)$, approaching a generic forest. The forest is characterized by a resistive body force

$$\mathbf{f} = -c_d a_f |\mathbf{U}| \mathbf{U}, \tag{1}$$

where c_d is the drag coefficient, a_f is the leaf-area density and $\mathbf{U} = (U, V, W)$ is the velocity vector in the x, y, z reference frame, with x, y and z indicating the streamwise, spanwise and vertical directions, respectively. For the sake of clarity, index notation will be used when convenient, with 1, 2 and 3 indicating the x, y and z components, respectively. All physical quantities are normalized by the density and a characteristic velocity and length scale (here, the freestream velocity, U_∞ , and the canopy height, h_c , respectively); the pressure is consequently scaled by ρU_∞^2 , the turbulent kinetic energy (TKE), k , with U_∞^2 and its rate of dissipation, ϵ , with U_∞^3/h_c .

The incompressible steady RANS equations are

$$\frac{\partial U_i}{\partial x_i} = 0, \tag{2}$$

$$U_j \frac{\partial U_i}{\partial x_j} = -\frac{\partial P}{\partial x_i} - \frac{\partial \overline{u'_i u'_j}}{\partial x_j} + \nu \frac{\partial^2 U_i}{\partial x_j^2} + f_i, \tag{3}$$

where the Reynolds stress term is modelled according to the Boussinesq hypothesis

$$\overline{u'_i u'_j} = \frac{2}{3} \delta_{ij} k - \nu_t \left(\frac{\partial U_i}{\partial x_j} + \frac{\partial U_j}{\partial x_i} \right), \tag{4}$$

with $k = (\overline{u'^2} + \overline{v'^2} + \overline{w'^2})/2$ representing the TKE, while ν and ν_t indicate the normalized kinematic viscosity and turbulent eddy viscosity, respectively. It is worth mentioning that the eddy viscosity is postulated on dimensional grounds to be of the form $\nu_t = C_\mu k^2/\epsilon$, where $C_\mu = 0.09$ (Silva Lopes et al. 2013). To complete the model, the equations for k and ϵ are chosen to be

$$U_j \frac{\partial k}{\partial x_j} = \frac{\partial}{\partial x_j} \left[\left(\nu + \frac{\nu_t}{\sigma_k} \right) \frac{\partial k}{\partial x_j} \right] + \mathcal{P} - \epsilon + S_k, \tag{5}$$

$$U_j \frac{\partial \epsilon}{\partial x_j} = \frac{\partial}{\partial x_j} \left[\left(v + \frac{v_t}{\sigma_\epsilon} \right) \frac{\partial \epsilon}{\partial x_j} \right] + C_{\epsilon 1} \frac{\epsilon}{k} \mathcal{P} - C_{\epsilon 2} \frac{\epsilon^2}{k} + S_\epsilon, \tag{6}$$

with the constants $\sigma_k = 1, \sigma_\epsilon = 1.22, C_{\epsilon 1} = 1.44, C_{\epsilon 2} = 1.92$ (Silva Lopes et al. 2013). The shear-production term is defined as $\mathcal{P} = -\overline{u'_i u'_j} (\partial U_i / \partial x_j)$ while the forest-related source terms in the $k - \epsilon$ equations are modelled as

$$S_k = -\beta_p c_d a_f |\mathbf{U}| k, \tag{7a}$$

$$S_\epsilon = -\beta_p C_{\epsilon 5} c_d a_f |\mathbf{U}| \epsilon, \tag{7b}$$

with $\beta_p = 4$ and $C_{\epsilon 5} = 0.9$, according to Silva Lopes et al. (2013).

Let us consider now the incoming boundary layer, $U_0(z)$, with characteristic $k_0(z)$ and $\epsilon_0(z)$ profiles. The undisturbed flow is here assumed to be parallel to the surface and thereby a function of z only. The terms \mathbf{f} , and S_k and S_ϵ represent perturbations to such an undisturbed state, generating a deviation from it; we indicate such perturbations with the superscript “(1)”, so that $U(x, y, z) = U_0(z) + U^{(1)}(x, y, z)$. By assuming now that the undisturbed flow satisfies Eqs. 2, 3, 5 and 6 and that $U^{(1)} \ll U_0$, it is possible to linearize Eqs. 2 and 3 to obtain

$$\frac{\partial U_i^{(1)}}{\partial x_i} = 0, \tag{8}$$

$$U_0 \frac{\partial U_i^{(1)}}{\partial x} + W^{(1)} \frac{dU_0}{dz} \delta_{i1} = -\frac{\partial P^{(1)}}{\partial x_i} - \frac{\partial \overline{u'_i u'_j}^{(1)}}{\partial x_j} + v \frac{\partial^2 U_i^{(1)}}{\partial x_j^2} + f_i, \tag{9}$$

where the perturbation Reynolds stress is given by

$$\overline{u'_i u'_j}^{(1)} = \frac{2}{3} \delta_{ij} k^{(1)} - v_{t0} \left(\frac{\partial U_i^{(1)}}{\partial x_j} + \frac{\partial U_j^{(1)}}{\partial x_i} \right) - v_t^{(1)} \frac{dU_0}{dz} (\delta_{i1} \delta_{j3} + \delta_{i3} \delta_{j1}). \tag{10}$$

As can be seen from Eq. 10, the perturbation terms generate a modification of the undisturbed turbulent eddy viscosity $v_{t0} = C_\mu k_0^2 / \epsilon_0$ into $v_t = v_{t0} + v_t^{(1)}$ where the linearized modification is given by

$$v_t^{(1)} = \left(C_\mu \frac{2k_0}{\epsilon_0} \right) k^{(1)} + \left(-C_\mu \frac{k_0^2}{\epsilon_0^2} \right) \epsilon^{(1)} = \psi_k(z) k^{(1)} + \psi_\epsilon(z) \epsilon^{(1)}, \tag{11}$$

where the sensitivity coefficients ψ_k and ψ_ϵ are given by the partial derivatives of v_t with respect to k and ϵ . By inserting Eq. 10 into Eq. 9, it is possible to obtain

$$U_0 \frac{\partial U_i^{(1)}}{\partial x} + W^{(1)} \frac{dU_0}{dz} \delta_{i1} = -\frac{\partial P^{(1)}}{\partial x_i} - \frac{2}{3} \frac{\partial k^{(1)}}{\partial x_i} + (v_{t0} + v) \frac{\partial^2 U_i^{(1)}}{\partial x_j^2} + \frac{dv_{t0}}{dz} \left(\frac{\partial U_i^{(1)}}{\partial z} + \frac{\partial W^{(1)}}{\partial x_i} \right) + \frac{\partial}{\partial z} \left(v_t^{(1)} \frac{dU_0}{dz} \right) \delta_{i1} + \frac{\partial v_t^{(1)}}{\partial x} \frac{dU_0}{dz} \delta_{i3} + f_i. \tag{12}$$

Both Eqs. 11 and 12 require knowledge of the perturbed TKE and dissipation. These can be obtained by linearizing the respective equations to

$$\begin{aligned}
 &U_0 \frac{\partial k^{(1)}}{\partial x} + W^{(1)} \frac{dk_0}{dz} \\
 &= \frac{1}{\sigma_k} \left[(v_{t0} + \sigma_k v) \frac{\partial^2 k^{(1)}}{\partial x_j^2} + \frac{dv_{t0}}{dz} \frac{\partial k^{(1)}}{\partial z} + \frac{\partial}{\partial z} \left(v_t^{(1)} \frac{\partial k_0}{\partial z} \right) \right] + \mathcal{P}_k^{(1)} + S_k, \quad (13)
 \end{aligned}$$

$$\begin{aligned}
 &U_0 \frac{\partial \epsilon^{(1)}}{\partial x} + W^{(1)} \frac{d\epsilon_0}{dz} \\
 &= \frac{1}{\sigma_\epsilon} \left[(v_{t0} + \sigma_\epsilon v) \frac{\partial^2 \epsilon^{(1)}}{\partial x_j^2} + \frac{dv_{t0}}{dz} \frac{\partial \epsilon^{(1)}}{\partial z} + \frac{\partial}{\partial z} \left(v_t^{(1)} \frac{\partial \epsilon_0}{\partial z} \right) \right] + \mathcal{P}_\epsilon^{(1)} + S_\epsilon, \quad (14)
 \end{aligned}$$

where the terms $\mathcal{P}_k^{(1)}$ and $\mathcal{P}_\epsilon^{(1)}$ are the production and dissipation terms for k and ϵ given by

$$\mathcal{P}_k^{(1)} = 2v_{t0} \frac{dU_0}{dz} \left(\frac{\partial U^{(1)}}{\partial z} + \frac{\partial W^{(1)}}{\partial x} \right) + \psi_k \left(\frac{dU_0}{dz} \right)^2 k^{(1)} + \left[\psi_\epsilon \left(\frac{dU_0}{dz} \right)^2 - 1 \right] \epsilon^{(1)}, \quad (15)$$

$$\mathcal{P}_\epsilon^{(1)} = C_{\epsilon 1} C_\mu \frac{dU_0}{dz} \left[2k_0 \left(\frac{\partial U^{(1)}}{\partial z} + \frac{\partial W^{(1)}}{\partial x} \right) + \frac{dU_0}{dz} k^{(1)} \right] + C_{\epsilon 2} \frac{\epsilon_0}{k_0} \left(\frac{\epsilon_0}{k_0} k^{(1)} - 2\epsilon^{(1)} \right). \quad (16)$$

Given the base flow U_0, k_0 and ϵ_0 , the solution of Eqs. 9, 12, 13 and 14 provides the additive correction to the base state able to account for the body force, \mathbf{f} , due to the canopy (and for its corresponding effect in the k and ϵ equations). Being rigorous and self-consistent in the derivation, the forcing terms should also be subjected to the linearization, so that $f_1 = -c_d a_f U_0^2 + \mathcal{O}(c_d a_f U_0 U^{(1)})$ and the first term only should be used to generate the first-order perturbation field. However, in the limit of a forest of infinite horizontal extent, the constant force $-c_d a_f U_0^2$ leads to an unphysical back-flow. This can be avoided by introducing higher-order corrections to the linearized problem. Alternatively, Belcher et al. (2003) suggested an iterative approach where $f_1 = -c_d a_f (U_0 + U^{(1)})^2$, whereby the order relationship is lost in the perturbation term; however, it has the advantage that, as the velocity magnitude is reduced by the drag of the forest, the same happens to the body force, which vanishes in the limit of a very long forest. In the present work the same philosophy is adopted, and the perturbation terms are therefore computed as

$$\mathbf{f} = -c_d a_f \left| \mathbf{U}_0 + \mathbf{U}^{(1)} \right| \left(\mathbf{U}_0 + \mathbf{U}^{(1)} \right), \quad (17)$$

$$S_k = -\beta_p c_d a_f \left| \mathbf{U}_0 + \mathbf{U}^{(1)} \right| \left(k_0 + k^{(1)} \right), \quad (18)$$

$$S_\epsilon = -\beta_p C_{\epsilon 5} c_d a_f \left| \mathbf{U}_0 + \mathbf{U}^{(1)} \right| \left(\epsilon_0 + \epsilon^{(1)} \right). \quad (19)$$

2.1 Numerical Implementation and Base Flow

Equations 9, 12, 13 and 14 were here solved by applying a Fourier transform in the horizontal plane, defined as

$$\hat{\phi}(\alpha, \beta; z) = \int_{\mathbb{R}^2} \phi(x, y, z) \exp[-i(x\alpha + y\beta)] dx dy, \quad (20)$$

with α and β indicating the streamwise and spanwise wavenumber, respectively.

Variations in the vertical direction were characterized by using Chebyshev polynomials (discretized with a Gauss-Lobatto distribution and mapped into the physical space by an exponential map of the form $\xi = A + Be^{-Cz}$, with A, B, C determined by the domain boundaries and the desired stretch of the grid near the surface), transforming the available set of differential equations into an algebraic linear system (Schmid and Henningson 2001). The use of the Fourier transform in the horizontal plane and of the Chebyshev polynomials in the vertical direction ensured a higher numerical accuracy compared to finite-difference schemes (Shen et al. 2011). Since the available LES data are statistically two-dimensional, the model was solved assuming $V^{(1)} = \overline{u'v'}^{(1)} = \overline{v'w'}^{(1)} = 0$ and for $\beta = 0$ only, reducing significantly the computational cost. Nevertheless, the extension to the three-dimensional case is straightforward. The grid in the streamwise direction was composed by 2048 grid points equally spaced between $-100h_c$ and $500h_c$, while 101 Chebyshev polynomials were used in the vertical direction. It is worth mentioning that the solution converged (within an error of 1%) already for a streamwise discretization composed of 512 grid points, corresponding to a total computational time of around 15 min on a standard desktop computer.

The use of the Fourier transform in the streamwise direction implied a periodicity of the inlet-outlet. If some streamwise momentum is extracted inside the domain (for instance by the canopy), then the flow momentum monotonically decreases and a steady state can thus be achieved only through the emergence of an artificial pressure gradient in the streamwise direction. In order to avoid this unphysical feature, a buffer zone was introduced between $400h_c$ and $490h_c$ where an artificial body force $f_1 = -\lambda(x)U^{(1)}$ was introduced (with $\lambda(x)$ proportional to the form proposed by Chevalier et al. (2007), which is zero outside the fringe domain) to force the velocity perturbation to vanish at the end of the domain. Similar considerations apply for the $k^{(1)}$ and $\epsilon^{(1)}$ source terms, leading to the expressions

$$\mathbf{f} = -c_d a_f \left| \mathbf{U}_0 + \mathbf{U}^{(1)} \right| \left(\mathbf{U}_0 + \mathbf{U}^{(1)} \right) - \lambda(x)\mathbf{U}^{(1)}, \tag{21}$$

$$S_k = -\beta_p c_d a_f \left| \mathbf{U}_0 + \mathbf{U}^{(1)} \right| \left(k_0 + k^{(1)} \right) - \lambda(x)k^{(1)}, \tag{22}$$

$$S_\epsilon = -\beta_p C_{\epsilon S} c_d a_f \left| \mathbf{U}_0 + \mathbf{U}^{(1)} \right| \left(\epsilon_0 + \epsilon^{(1)} \right) - \lambda(x)\epsilon^{(1)}. \tag{23}$$

The boundary conditions imposed on the perturbations were

$$U^{(1)} = V^{(1)} = W^{(1)} = \frac{\partial W^{(1)}}{\partial z} = \frac{\partial k^{(1)}}{\partial z} = \frac{\partial \epsilon^{(1)}}{\partial z} = 0 \quad \text{at } z = z_0, \tag{24}$$

$$U^{(1)} = V^{(1)} = \frac{\partial W^{(1)}}{\partial z} = P^{(1)} = k^{(1)} = \epsilon^{(1)} = 0 \quad \text{as } z \rightarrow \infty. \tag{25}$$

Due to the choice of the logarithmic velocity profile, the no-slip condition must be applied at $z = z_0$ rather than at the ground. However, as the roughness length, z_0 , is usually very small, this approximation is not expected to play a significant role, unless the region very near the ground is of interest. On the other hand, since the domain size is finite, the infinity condition is imposed at $z = 100h_c$.

The adopted base flow should be a solution of the RANS equations with the $k - \epsilon$ closure in order to be consistent with the fully non-linear solution in the limit of small perturbations (although this is not a stringent requirement). The base flow is here assumed to be described by

$$U_0(z) = \frac{u_*}{\kappa} \ln \left(\frac{z}{z_0} \right), \tag{26a}$$

$$k_0 = \frac{u_*^2}{\sqrt{C_\mu}}, \tag{26b}$$

$$\epsilon_0 = \frac{u_*^3}{\kappa z}, \tag{26c}$$

where u_* and κ are the friction velocity (normalized by the chosen characteristic velocity and length scale) and von Kármán constant, respectively. The base state (26a–26c) is a solution of the RANS equations with the $k - \epsilon$ closure if $\kappa^2 = \sigma_\epsilon (C_{\epsilon 2} - C_{\epsilon 1}) \sqrt{C_\mu}$, a requirement that would imply $\kappa = 0.419$ with the adopted set of constants. However, the value of $\kappa = 0.4$ was adopted in the present work, so that the ϵ equation is slightly violated by the choice of the basic state, although the discrepancies are expected to be negligible away from the ground. With this choice of base state, the expressions of the turbulent eddy viscosity and its sensitivity to k and ϵ variation are given by

$$v_{t0} = \kappa u_* z, \tag{27a}$$

$$\psi_k = 2\sqrt{C_\mu} \frac{\kappa z}{u_*}, \tag{27b}$$

$$\psi_\epsilon = - \left(\frac{\kappa z}{u_*} \right)^2. \tag{27c}$$

3 LES Set-Up

Several LES have been performed so as to validate the model for with different forest configurations. The governing equations are obtained by applying a spatial filter to the Navier–Stokes equations as

$$\frac{\partial \tilde{u}_i}{\partial t} + \tilde{u}_j \frac{\partial \tilde{u}_i}{\partial x_j} = - \frac{\partial \tilde{p}}{\partial x_i} + \frac{1}{Re} \frac{\partial^2 \tilde{u}_i}{\partial x_j^2} + \frac{\partial \tau_{ij}^{SGS}}{\partial x_j} - c_d a_f |\tilde{\mathbf{u}}| \tilde{u}_i, \tag{28}$$

where the tilde denotes filtered quantities. The Reynolds number is defined as $Re = U_\infty \delta / \nu$, where U_∞ is the freestream velocity, δ is the 99 % boundary-layer thickness and here ν is the kinematic viscosity of the air. In the present simulations $Re = 3.8 \times 10^4$, which was the highest possible value achievable with the available computational resources.

The eddy-viscosity model was used to close the subgrid-stress (SGS) tensor τ_{ij}^{SGS} as

$$\tau_{ij}^{SGS} = \nu_T^{SGS} \left(\frac{\partial \tilde{u}_i}{\partial x_j} + \frac{\partial \tilde{u}_j}{\partial x_i} \right), \tag{29}$$

where, ν_T^{SGS} indicates the SGS eddy viscosity.

The Non-Rotating Coherent-structure Smagorinsky Model (NRCSM, Kobayashi 2005) was used in the present simulations: here the eddy viscosity in the NRCSM is calculated as

$$\nu_T^{SGS} = C_s \|F_{CS}\|^{3/2} \Delta^2 \sqrt{2S_{ij}S_{ij}}, \tag{30}$$

where S_{ij} is the strain-rate tensor, the constant C_s in the NRCSM is 0.05 and F_{CS} is the coherent-structure function. The coherent-structure function is calculated as $F_{CS} = Q/E$, where Q is the second invariant of the velocity-gradient tensor. The denominator of the coherent-structure function, E , is calculated as

$$E = \frac{1}{2} (W_{ij}W_{ij} + S_{ij}S_{ij}), \tag{31}$$

where W_{ij} is the rotation tensor.

3.1 Numerical Set-Up

As illustrated in Fig. 1, the computational domain is composed of two parts, similar to Lund et al. (1998): one is a driver part, where the neutral boundary-layer inflow is generated by recycling the properly rescaled velocity profiles at the recycling station, and the other is the main part, where the canopy and the clearings are located. The velocity rescaling at the driver part is calculated as

$$u_{inlt} = \gamma [U_{recy}^{inn} + u'_{recy}{}^{inn}] [1 - W(\eta_{inlt})] \gamma [U_{recy}^{out} + u'_{recy}{}^{out}] W(\eta_{inlt}), \tag{32}$$

where capital letters indicate quantities averaged in time, while the primes mark the fluctuation from the time-mean value. The subscripts \cdot_{inlt} and \cdot_{recy} denote the value at the inlet and at the recycle plane, respectively, and the superscripts \cdot^{inn} and \cdot^{out} indicate with which scale the velocity is non-dimensionalized, the inner scale or the outer scale η . Here, γ is the ratio of the friction velocity between the inlet and the recycling station and $W(\eta)$ is a weighting function; this is a hyperbolic tangent-type function that is used to blend the rescaled quantities. With respect to the original recycle method proposed by Lund et al. (1998), two of the modifications suggested by Jewkes et al. (2011) are applied. The first modification is the use of the displacement thickness, i.e., $\delta^* = \int_0^\infty (1 - U/U_\infty) dz$, as an outer length scale instead of the 99% boundary-layer thickness, δ , so that the inlet mass flux is more stable. The second modification applies mirroring to the rescaled profile in order to avoid spurious structure.

The size of each domain ($L_x \times L_y \times L_z$) is $(3\pi\delta \times \pi\delta \times 5\delta \approx 90h_c \times 15h_c \times 50h_c)$, where L represents the length in each direction, and the number of grid points ($N_x \times N_y \times N_z$) is $(256 \times 256 \times 98)$ for both the main and driver parts. The grid size in wall units ($\Delta x^+ \times \Delta y^+ \times \Delta z_{min}^+$) is $(55.6 \times 18.5 \times 0.8)$; a hyperbolic tangent-type stretching is used in the wall-normal direction below $z/\delta = 1$.

The second-order accurate finite difference method is used in the LES code, which is based on the direct numerical simulation (DNS) code of Kametani and Fukagata (2011). A staggered grid system, where the velocities are defined on the cell surface, while the pressure and the eddy viscosity are located at the cell centre, is used in the present model. Equation 28 is temporally integrated using a low-storage third-order accurate Runge–Kutta/Crank–Nicolson scheme, while a divergence-free condition for the velocity is imposed by coupling the pressure field with the velocity. The coupling is done by solving the Poisson equation of the pressure.

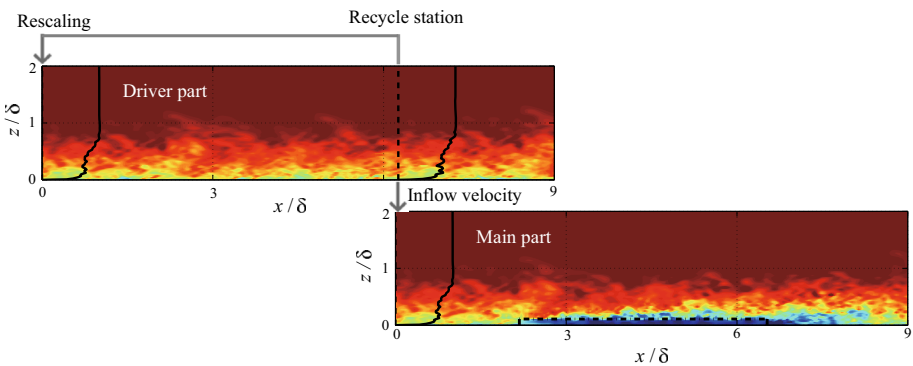


Fig. 1 The driver part and the main part used for LES. The colours denote the instantaneous streamwise velocity component in a cross-section (red high; blue low). The dash-dotted line in the main part represents the canopy. Note that here x , z and δ are non-dimensional and scaled by h

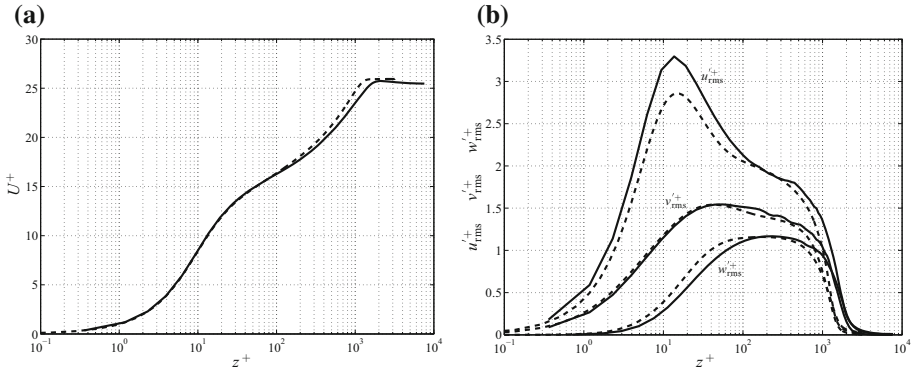


Fig. 2 Statistics computed by the present LES at $Re \approx 4 \times 10^4$ ($Re_\theta \approx 4000$) in the case without a canopy: **a** mean velocity profile; **b** r.m.s. of the velocity fluctuations. (Solid line) present LES; (dashed line) DNS of Schlatter and Örlü (2010)

In both the driver and the main domains, the upper boundary conditions for the streamwise velocity component u , the vertical velocity component w , and the spanwise velocity component v are imposed as $\partial u/\partial z = \partial v/\partial z = w = 0$, while the no-slip condition is imposed at the ground surface boundary. A constant mass flux is applied at the inflow boundaries. The advective boundary condition of Miyauchi et al. (1994) is applied at the downstream end of each computational domain, while periodic boundary conditions are imposed at the spanwise boundaries.

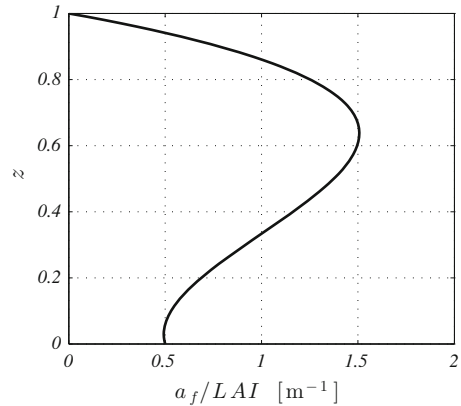
The flow field of a turbulent boundary layer at a low Reynolds number (with friction Reynolds number of $Re_\tau = u_\tau \delta/\nu \approx 180$, which corresponds to $Re = U_\infty \delta/\nu \approx 3000$), originally used in the DNS code of Kametani and Fukagata (2011), was used as the initial field. The non-dimensional timestep $\Delta t U_\infty/\delta$ was set to be 1×10^{-3} . Pre-computations were continued until $T \approx 100 U_\infty/\delta$, at which the flow is assumed to have reached the statistically steady regime. After this pre-computation, the first- and the second-order statistics were computed every 50 timesteps, and iterations were done until 50,000 time-steps.

Figure 2 shows the statistics computed by the present LES at $Re \approx 4 \times 10^4$ (corresponding to a momentum-thickness-based Reynolds number of $Re_\theta \approx 4000$) in the case without a canopy. It can be noted that both the mean velocity profile and the root-mean-square velocity fluctuations are fairly well reproduced as compared to the DNS data (Schlatter and Örlü 2010), although a small amount of insufficient redistribution among velocity components can be found in Fig. 2b. Note that in Fig. 2 (and only there) the + superscript indicates viscous scaling, namely z scaled by ν/u_* and the velocities scaled by u_* .

3.2 Forest Set-Up

The boundary-layer profile at the inlet of the LES was characterized as $U = (u_*/\kappa) \ln(z/z_0)$ with $z_0/h_c = 0.00075$ and $u_*/U_\infty = 0.0384$, providing the parameters for the base flow in the mathematical model. On the other hand, the canopy body force was characterized by the product of the drag coefficient and the leaf-area density. The former was assumed to be constant ($c_d = 0.2$) while the latter was assumed to have the shape shown in Fig. 3 (similarly to Dupont and Brunet 2009) normalized by the leaf-area index (LAI), defined as $LAI = h_c \int_0^1 a_f dz$. The LAI values were changed from 0.05 to 5 in the RANS simulations

Fig. 3 Leaf-area density (a_f) normalized by the leaf-area index (LAI)



(both linear and non-linear), while only two LAI values were used in the LES, namely $LAI = 2$ and $LAI = 5$.

The full-forest configuration was two-dimensional and rectangular starting from $x = 0$ and terminating at $x = 40h_c$. Four different clearing configurations were considered, where a clearcut was added between $20 \leq x/h_c \leq 25$, $20 \leq x/h_c \leq 30$, $20 \leq x/h_c \leq 35$ and for $x/h_c \geq 20$ (the latter representing just a shorter full forest).

4 Non-linear RANS Simulations

The model developed in Sect. 2 is based on a linearized solution of the RANS equations with a linearized $k - \epsilon$ model for the turbulence closure, mimicking the non-linear code, but faster. In the best-case scenario, the model provides a solution of the non-linear RANS equations. Therefore, any discrepancy observed when comparing with LES might be due to both the linearization and the $k - \epsilon$ model error. In order to distinguish between the two error sources or (at least) to qualitatively assess their importance, additional non-linear RANS simulations were performed by means of OpenFOAM, a code based on a finite-volume approach. The 2D computational domain was $600h_c$ long and $50h_c$ high discretized into 1000 and 200 segments, respectively. The same inlet boundary layer of the linearized simulation was imposed as an inlet condition, while the lower boundary was described by wall functions. The scheme proposed by Silva Lopes et al. (2013) for the source terms in the k and ϵ equations was also adopted. The same homogeneous forest used in the linearized RANS and LES was studied, but with a wider range of LAI to characterize the departure from the linear behaviour.

Figure 4 shows the comparison of the main characteristic variables U , k and ϵ in the middle of the canopy and just above it ($x = 20h_c$, $z = 1.5h_c$). From now on, the statistics are normalized with U_∞ and h_c , although the scaling is removed from the figure labels and caption for the sake of clarity. The comparison shows that the linear model is able to replicate qualitatively only the mean velocity, while the turbulence quantities are severely underestimated. The error in k is distributed amongst the three velocity variances (shown in Fig. 5), although the shear stress is surprisingly well estimated. By comparing the present model with the mixing-length-based model proposed by Belcher et al. (2003), it is quite clear that the linearization is still valid for the momentum equation, but cannot be extended with confidence to the k and ϵ equations. A possible reason for the different agreements is due to the fact that the $U^{(1)}$ correction is smaller than $U_0(z)$, while $k^{(1)}$ and $\epsilon^{(1)}$ can be several times

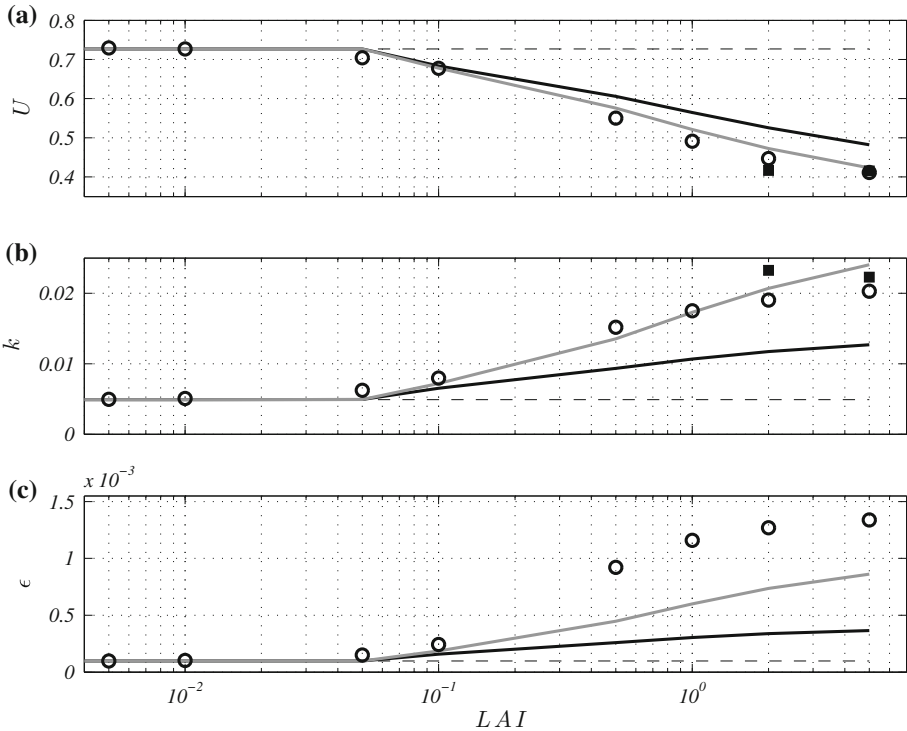


Fig. 4 Comparison of U , k and ϵ at $x = 20h_c$ and $z = 1.5h_c$ between the linearized model (solid black line) against non-linear RANS data (circles) for different LAI . The grey lines indicate the linear model corrected with the second-order correction, while the dashed lines indicate the undisturbed values. The black squares are the corresponding LES data

larger than their undisturbed counterparts. Nevertheless, an expansion in terms of turbulent viscosity seems to be still appropriate as most of the diffusive processes are still dominated by the unperturbed turbulent eddy viscosity (justifying the agreement seen by Belcher et al. 2003).

A possible alternative to improving the estimated TKE is to develop a second-order correction that accounts for the non-linearities. The developed second-order correction is described in Appendix 1 and its effects can be seen in Figs. 4, 5 and 6 (for $LAI = 1$) marked by the grey lines. The second-order correction, however, overestimates k because of the non-linearity, so that an arbitrary factor of 2 is introduced to reduce the intensity of the second-order correction only: therefore, its use should be limited to the correction of k and to the determination of the velocity variances, when needed.

5 Results

The velocity statistics obtained for the full-forest configuration are shown in Fig. 7 where the proposed model is compared with the LES data for LAI values of 2 and 5 that, from now on, are studied in the present section (it is worth noting that all physical quantities are normalized by the density, the freestream velocity, U_∞ , and the canopy height, h_c , consistent

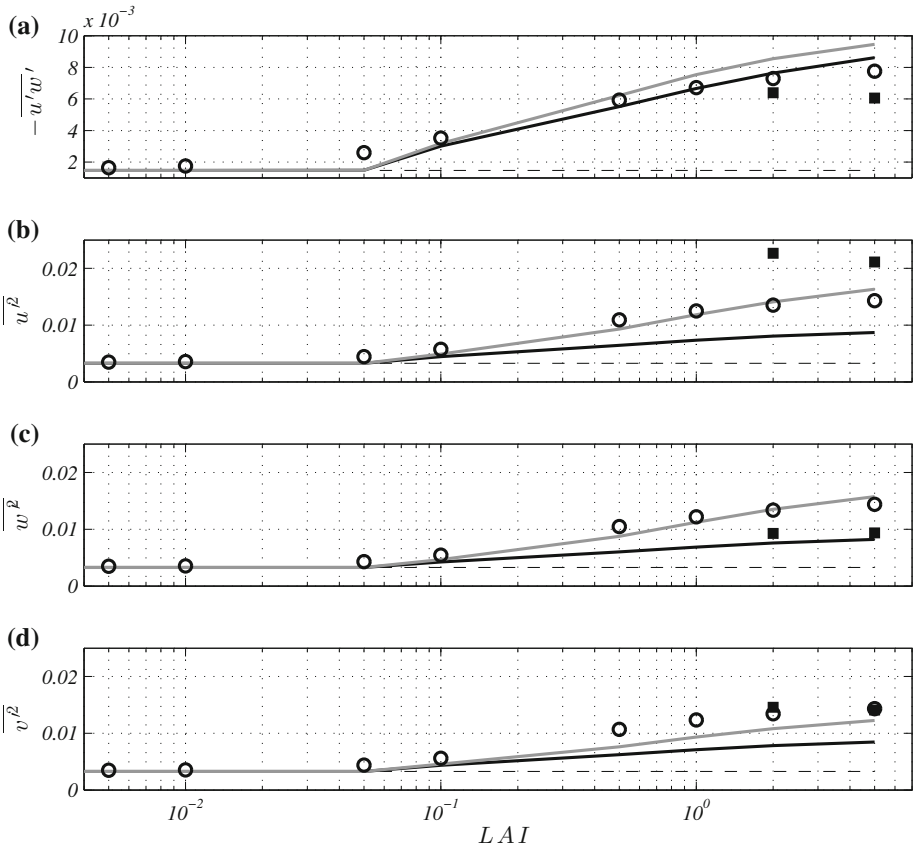


Fig. 5 Comparison of $-\overline{u'w'}$, $\overline{u'^2}$, $\overline{w'^2}$ and $\overline{v'^2}$ at $x = 20h_c$ and $z = 1.5h_c$ between the linearized model (solid black line) against non-linear RANS data (circles) for different LAI values. The grey lines indicate the linear model corrected with the second-order correction, while the dashed lines indicate the undisturbed values. The black squares are the corresponding LES data

with Sect. 2). The incoming logarithmic velocity profile is gradually modified downwind of the forest edge, with the characteristic flow deceleration inside the forest and the inflection point of the wind-speed profile occurring at the canopy top. The model adjusts to the forest condition less rapidly than does the LES (as visible, for instance, at $x = 10h_c$ and $x = 50h_c$), but both tend to the same nearly-parallel state. After the forest trailing edge, the wake of the forest provides velocity recovery near the ground, a dynamic that is accounted for by the first-order model as well. The same kind of agreement was reported by Belcher et al. (2003) when comparing the mean velocity profile estimated with the mixing-length-based linearized model with available RANS and experimental data. The Reynolds shear stress $\overline{u'w'}$ is then shown and it can be noted that it is slightly overestimated by the model over the canopy but nevertheless there is a qualitative agreement. For both the reported LAI values, the peak stress is located at the canopy top, vanishing both inside the canopy and away from it, as suggested by observations (Harman and Finnigan 2007; Segalini et al. 2013). The comparison of the $\overline{u'w'}$ profile upstream of the canopy and over it clearly shows the significant enhancement in the turbulence activity typically observed over forested areas, while the wake of the forest

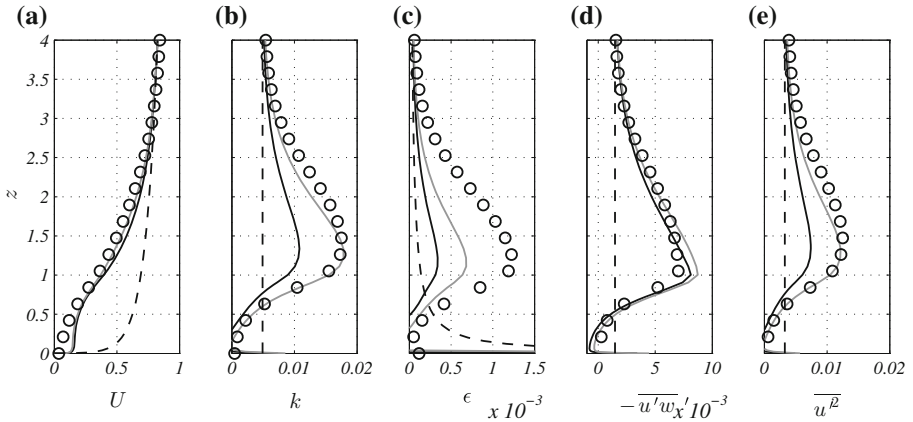


Fig. 6 Profiles at $x = 20h_c$ of U , k , ϵ , $-\overline{u'w'}$ and $\overline{u'^2}$ according to the linearized model (solid black line), non-linear RANS data (circles) for $LAI = 1$. The grey lines indicate the linear model corrected with the second-order correction, while the dashed lines indicate the undisturbed profiles

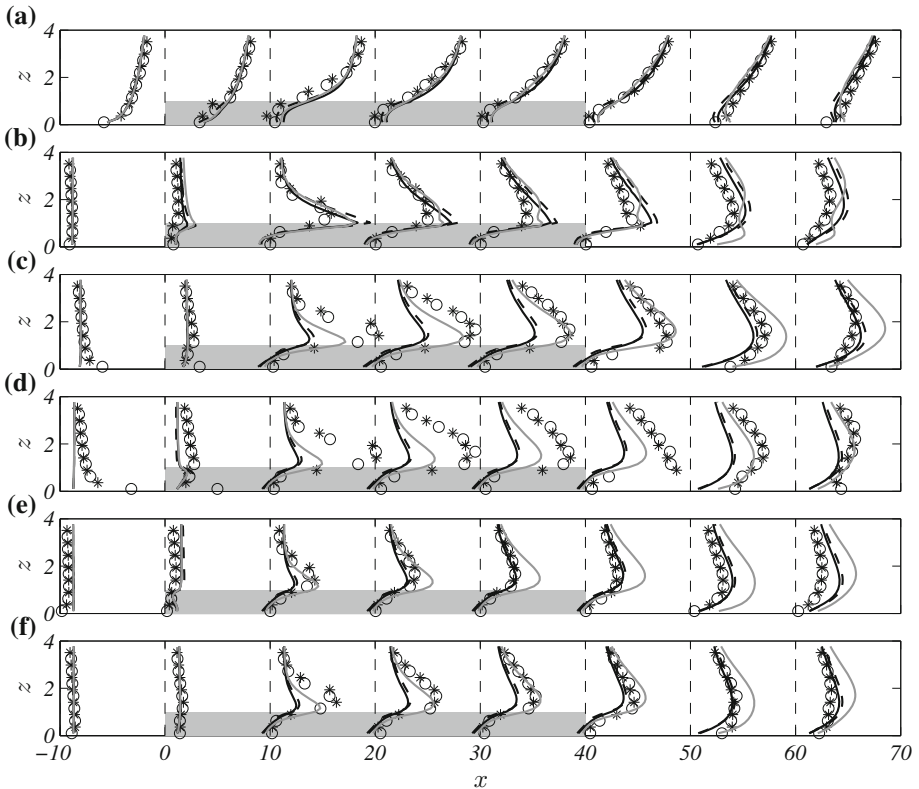


Fig. 7 Velocity statistics for the full-forest configuration. (a) $10U$, (b) $-800\overline{u'w'}$, (c) $400k$, (d) $400\overline{u'^2}$, (e) $400\overline{w'^2}$, (f) $400\overline{v'^2}$. Circles and asterisks indicate LES data for $LAI = 2$ and $LAI = 5$, respectively. Solid black lines and dashed lines indicate the corresponding first-order model results. The grey lines indicate the statistics calculated by means of the second-order model. The thin vertical dashed lines indicate the x -position where the quantities are evaluated

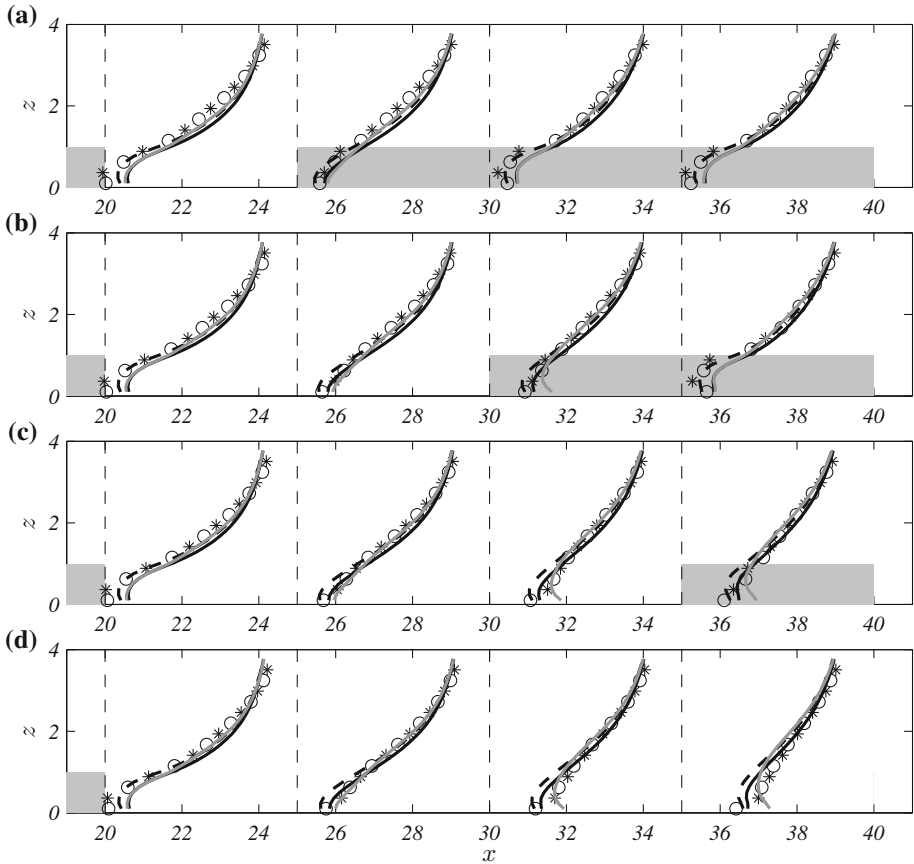


Fig. 8 U (scaled by a factor 5) for the four different forest configurations (the presence of the forest is indicated by a shaded area). See Fig. 7 for the used list of symbols

is quite persistent and the $\overline{u'w'}$ Reynolds stress component does not decay as rapidly as it increased upstream of the forest edge.

Some discrepancy is instead observed in the TKE, which is significantly underestimated by the first-order model by almost a factor of two over the canopy, while the disagreement decreases in the wake of the forest. Interestingly, by computing the normal Reynolds stresses, it is evident that most of the discrepancy is due to the underestimation of $\overline{u'^2}$, while $\overline{w'^2}$ is reasonably well characterized and $\overline{v'^2}$ is less severely underestimated over the forested area). The use of the second-order correction, discussed in Sect. 4 and Appendix 1, is beneficial and improves the estimation of the TKE and velocity variances significantly.

The LAI range used in Fig. 7 has a negligible effect on all the available statistics: actually this could have been anticipated from Figs. 4 and 5 where the statistics scale logarithmically with the leaf-area index for $LAI \gg 0.5$ (it should be, however, kept in mind that the threshold for the onset of the logarithmic behaviour depends on the length of the canopy as well), so forest-density effects will not be discussed further for the available LES, although data for both LAI values will be shown for the sake of completeness. Furthermore, this will allow

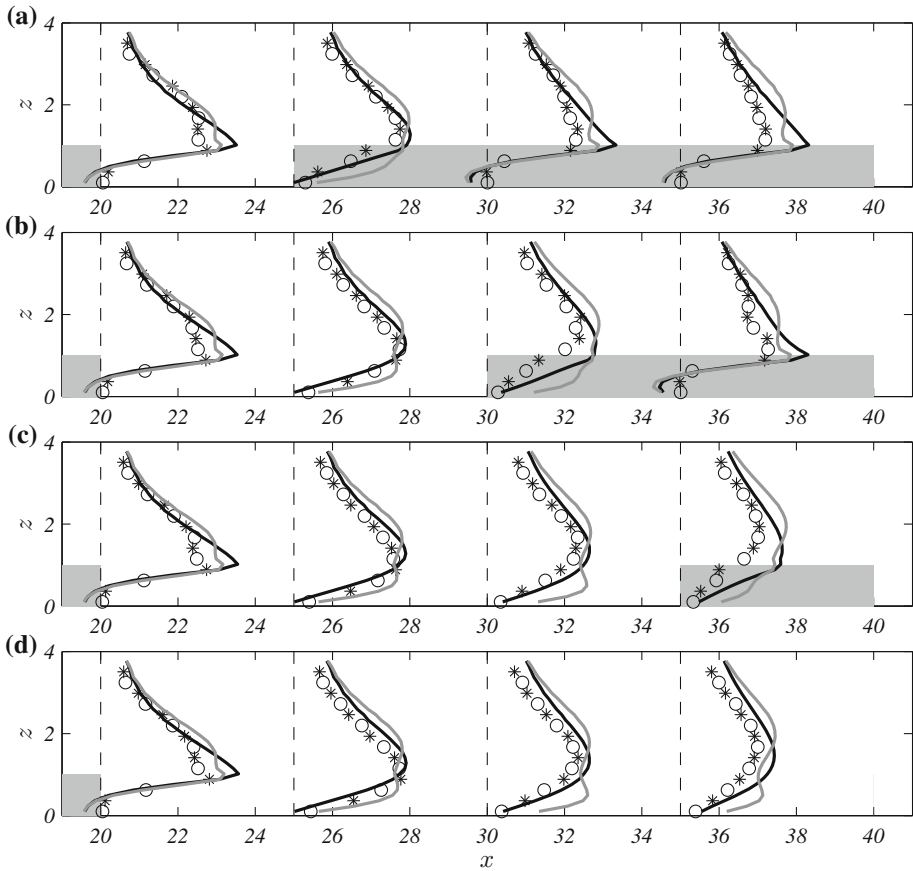


Fig. 9 $-\overline{u'w'}$ (scaled by a factor 400) for the four different forest configurations (the presence of the forest is indicated by a shaded area). See Fig. 7 for the used list of symbols

us to see whether or not the flow over clearings is as insensitive to the forest density as in the homogeneous forest case.

The velocity statistics for the various clearing configurations are now shown in Figs. 8, 9, 10, 11, 12 and 13. Similar to the homogeneous case, the mean velocity profile is properly estimated by the first-order model, showing the right recovery from the rough-to-smooth region and vice versa. For a short clearing the velocity is practically unchanged, while the deviation (or flow recovery) increases nearly linearly with the streamwise extent of the clearing. It was thought that a linear additive correction (able to estimate the clearing perturbation superposed to the full-forest condition) was possible, but the deviations were not self-similar between different clearing lengths and LAI . This is consistent with the analytic theory where the mean flow is obtained through the convolution of the roughness height with an opportune kernel, leaving out possible self-similar effects for short clearings, while long clearings are mostly dominated by the wake decay and by the rapid flow distortion near the trailing edge of the clearing.

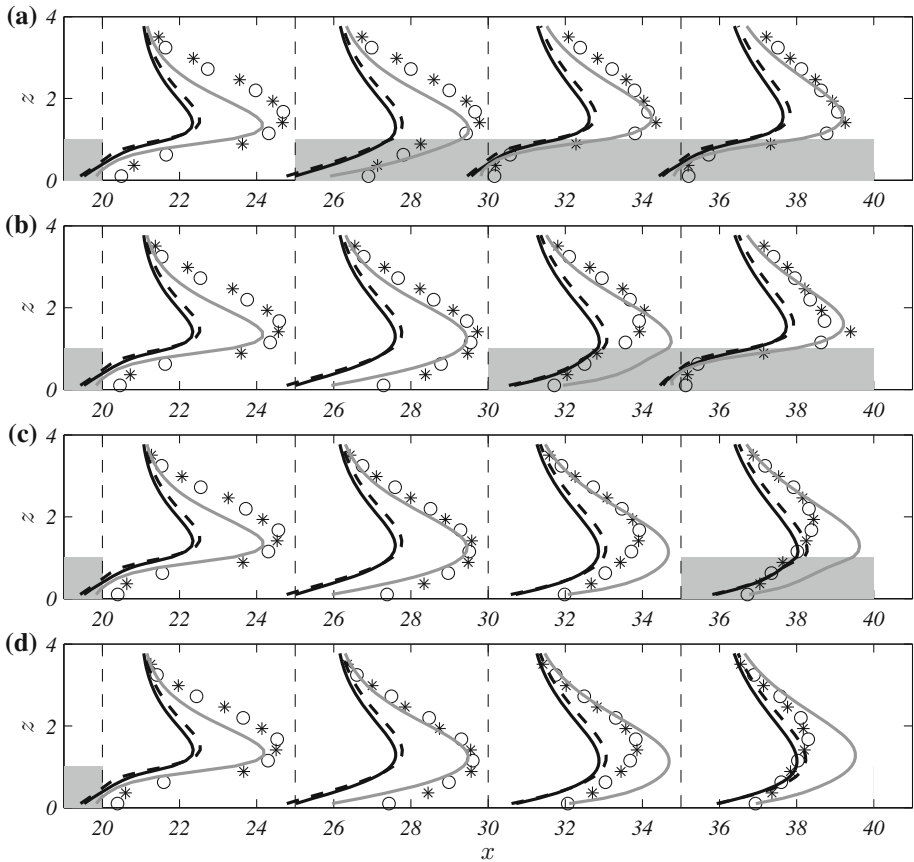


Fig. 10 k (scaled by a factor 200) for the four different forest configurations (the presence of the forest is indicated by a shaded area). See Fig. 7 for the used list of symbols

Figure 9 shows the modification of the shear stress $\overline{u'w'}$ with various clearing configurations, with a reasonable agreement between LES and the linearized model. The sudden interruption of the forest is perceived by the linearized method and the shear-stress profile changes concavity significantly, especially below the canopy top. When the forest restarts, the model is slower to recover than the LES, as noted before for the streamwise velocity component. It is of interest to point out that the linearized model overestimates the shear stress near the canopy top, while the LES data have a plateau in $\overline{u'w'}$ above the forest.

Figure 10 shows the TKE profiles from both LES and the linearized model, while all normal Reynolds stresses are shown in Figs. 11, 12 and 13. Consistent with the full-canopy analysis, both k and $\overline{u'^2}$ are underestimated by the first-order model by almost a factor of 2, while $\overline{w'^2}$ and $\overline{v'^2}$ are reasonably well estimated, although $\overline{v'^2}$ is still underestimated over the forested area and in the clearing area. Again the second-order correction improves the predictions of the first-order linearized model, although $\overline{u'^2}$ remains underestimated: this latter discrepancy is however due to a limitation of the non-linear $k - \epsilon$ model since the non-linear RANS simulations show a similar discrepancy (see Fig. 5).

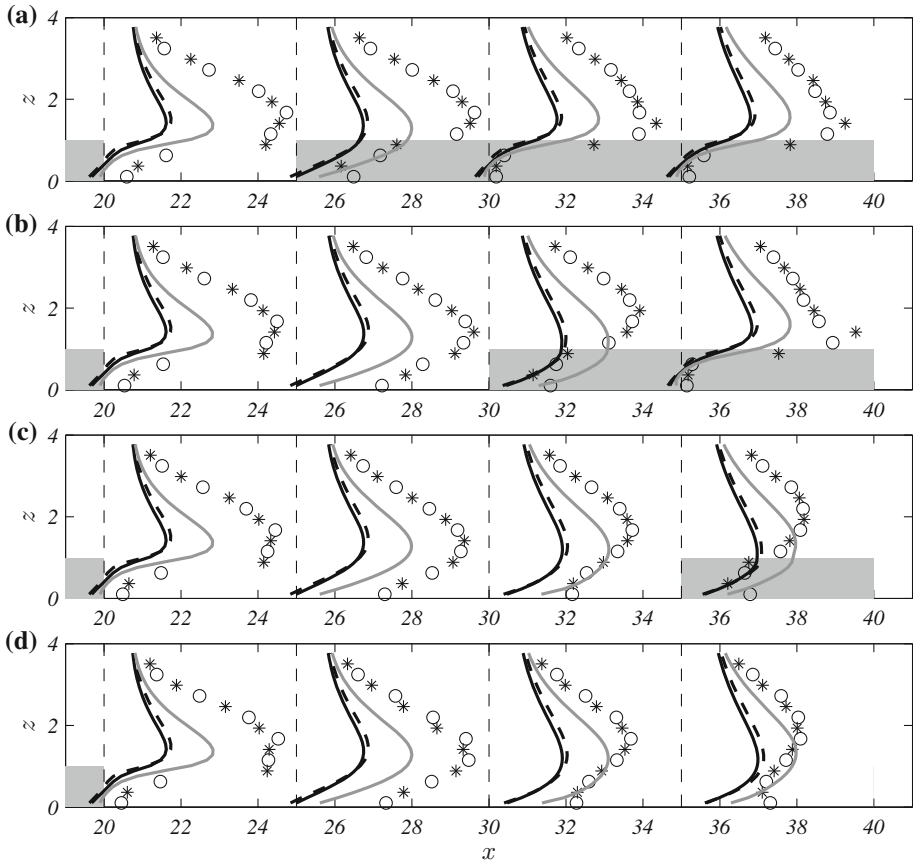


Fig. 11 $\overline{u'^2}$ (scaled by a factor 200) for the four different forest configurations (the presence of the forest is indicated by a shaded area). See Fig. 7 for the used list of symbols

6 Conclusions

A new simplified model has been proposed here to estimate the flow around forested areas based on a linearization of the RANS equations with a $k - \epsilon$ closure scheme. The linearization is performed around the incoming boundary layer (here characterized by the aerodynamic roughness length and friction velocity) perturbed by a body-force distribution to mimic the forest effects. The main advantage of the proposed linearization is the possibility of solving the RANS equations much more rapidly than non-linear simulations and much more accurately than finite-difference based schemes (Shen et al. 2011) with the drawback that a linearization error must be accounted for. As discussed earlier, in the limit of infinitely weak forest, the linearized RANS solution converges to a full non-linear RANS solution, while some deviations are observed for forests with large enough LAI (here the deviations are observed from LAI > 0.5, although that strongly depends on the length of the forest). It is expected that a complete analytical solution of the linearized RANS equations might be possible by enforcing the boundary-layer approximation (namely by accounting only for the turbulent momentum transfer in the vertical direction), but this possibility was not investigated in the present work.

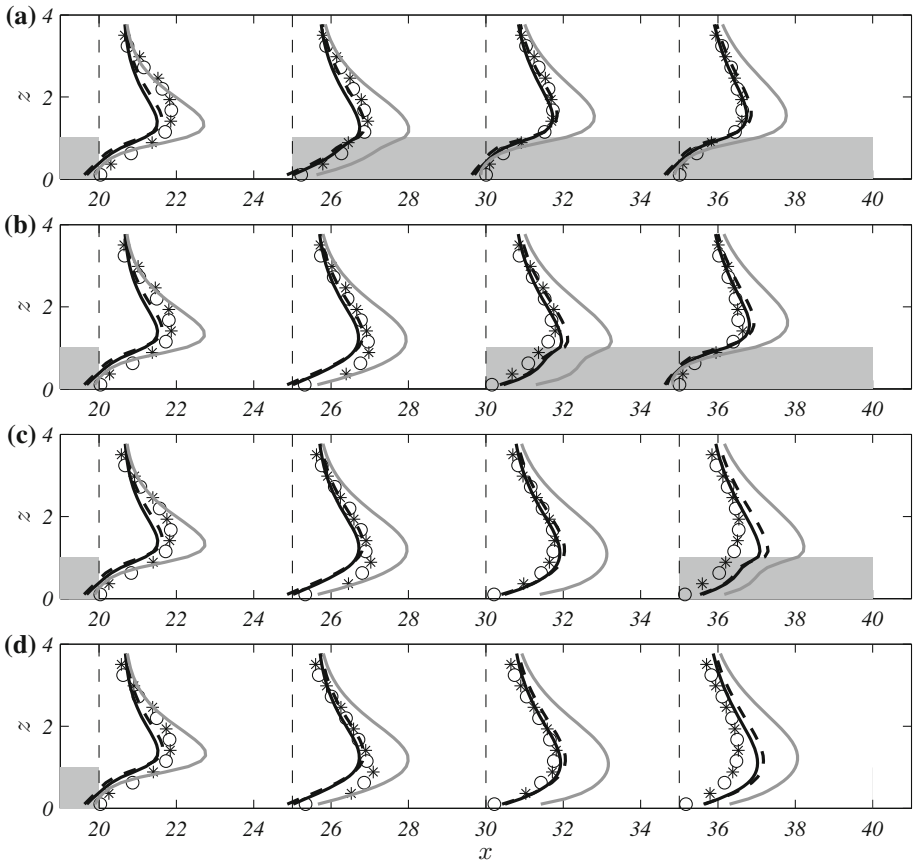


Fig. 12 $\overline{w'^2}$ (scaled by a factor 200) for the four different forest configurations (the presence of the forest is indicated by a shaded area). See Fig. 7 for the used list of symbols

The $k - \epsilon$ closure was preferred compared to a traditional mixing-length model since it does not need an estimation of the mixing length as with, for instance, the analytical model of Belcher et al. (2003), although the results are qualitatively similar in terms of the mean velocity profile and Reynolds stress $\overline{u'w'}$. Another advantage of the higher-order closure scheme is the possibility of estimating the Reynolds stress tensor beyond the shear stress $\overline{u'w'}$ (which is already provided by the mixing-length closures). The k and ϵ transport equations were here modified to account for the turbulence destruction caused by the forest, according to the suggestions of Silva Lopes et al. (2013). The values of the closure coefficients were the same as those used by Silva Lopes et al. (2013) in their comparison between RANS simulations and LES. Several non-linear RANS simulations were conducted for a full-forest configuration to assess the error due to the linearization of the RANS equations. The results demonstrated that the discrepancy increases as the LAI increases, although several quantities were less affected than others: for instance, the mean velocity and shear stress $\overline{u'w'}$ were reasonably well estimated, while the turbulent kinetic energy and velocity variances were severely underestimated. A second-order correction to the linear approach was then developed to remedy the poor agreement in the TKE, but its magni-

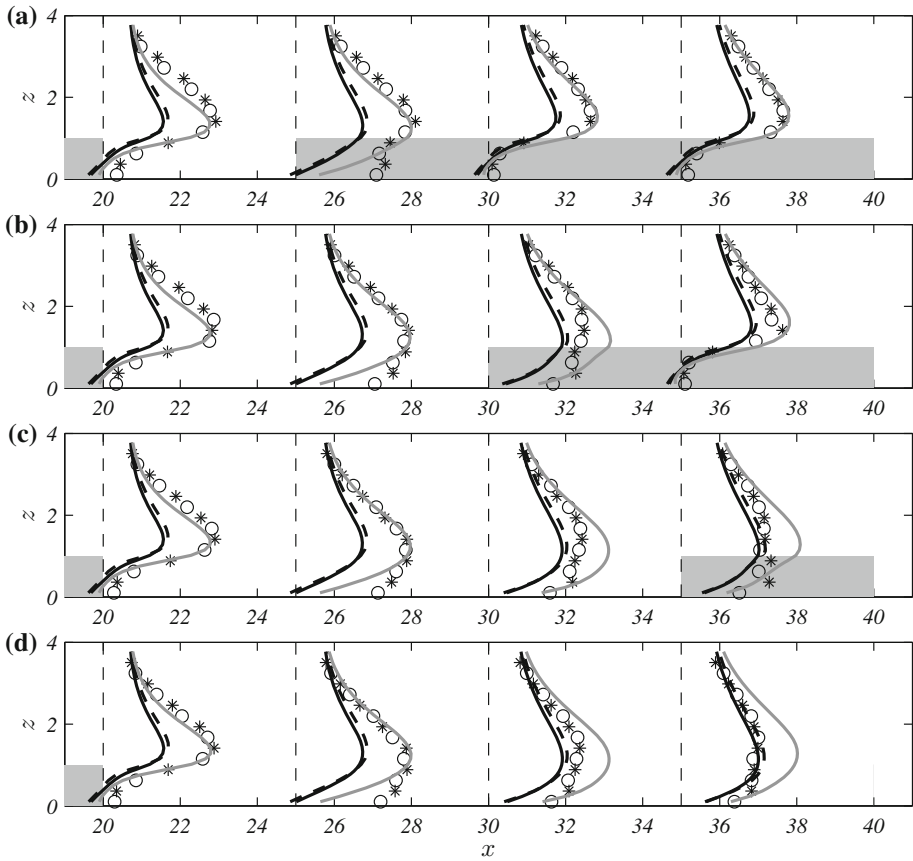


Fig. 13 $\overline{v'^2}$ (scaled by a factor 200) for the four different forest configurations (the presence of the forest is indicated by a shaded area). See Fig. 7 for the used list of symbols

tude was then too high and an empirical factor of two had to be introduced to attenuate the correction magnitude. Consequently, the use of the second-order correction is suggested only when the access to the velocity variances is desired, while the first-order approach (or the traditional mixing-length-based method) should be used if the mean velocity only is of interest.

Several large-eddy simulations were performed for different clearing configurations by introducing a body force in the momentum transport equations to simulate the forest, without directly changing the subgrid-stress model (similar to Dupont and Brunet 2009). A comparison between the LES results and the proposed first-order linearized model for realistic forest configurations has shown that the latter was able to estimate the mean streamwise velocity component, U , the shear stress, $\overline{u'w'}$ and the lateral normal stresses, $\overline{v'^2}$ and $\overline{w'^2}$, while it significantly overestimated the streamwise velocity variance, $\overline{u'^2}$, and consequently the TKE. The proposed second-order correction improved the agreement between the modelled and simulated TKE and $\overline{u'^2}$, although the introduction of the empirical factor of two makes the correction less trustworthy. Nevertheless, even the first-order approach improved existing simplified methodologies to assess forest effects with and without clearings, providing a

leading-order analysis of the canopy flow. It is unclear if the inclusion of higher-order terms in the expansion could improve the comparison, although it is expected to be beneficial since the fully non-linear RANS results showed a better agreement with the TKE calculated from LES. Since U and $\overline{u'w'}$ agree reasonably well, the role of the different closure methods (between RANS and LES) is marginal as most of the discrepancies arise from the linearization. The factor of two introduced for the second-order correction suggests that a higher-order correction should probably be pursued to properly account for the non-linearity, but this might not be worthwhile. Nevertheless, the first-order model remains a useful tool for weak and dense canopies (the latter necessitates the use of the second-order correction), but it could also be a feasible approach to simulate wind farms as the equivalent LAI is much smaller there.

Acknowledgments This work is part of Vindforsk IV, a research program sponsored by the Swedish Energy Agency as well as *STandUP for Wind*. Part of this work was done in the framework of Keio University-KTH double-degree program. The authors are grateful to Prof. P. Henrik Alfredsson (KTH) and Shinnosuke Obi (Keio University) for fruitful discussion. Niclas Berg (KTH) is greatly acknowledged for the help in setting up the RANS simulations with OpenFOAM.

Open Access This article is distributed under the terms of the Creative Commons Attribution 4.0 International License (<http://creativecommons.org/licenses/by/4.0/>), which permits unrestricted use, distribution, and reproduction in any medium, provided you give appropriate credit to the original author(s) and the source, provide a link to the Creative Commons license, and indicate if changes were made.

Appendix 1: Second-order correction

To improve the agreement between the first-order model, the non-linear RANS and LES results, a second-order correction has been developed by assuming an asymptotic expansions of the form

$$\mathbf{U} = \mathbf{U}_0(z) + \mathbf{U}^{(1)} + \mathbf{U}^{(2)}, \tag{33}$$

for the momentum and similarly for the pressure, TKE and TKE dissipation. The second-order correction should be small compared to the first, so that $\mathcal{O}(U^{(2)}) \ll \mathcal{O}(U^{(1)}) \ll \mathcal{O}(U_0)$. Consistently with the linearization, the products $\mathcal{O}(U^{(1)}U^{(1)})$ and $\mathcal{O}(U_0U^{(2)})$ will be considered to be of the same order of magnitude, while the other products will be neglected. The resulting second-order problem is still linear in the corrective term and it is the same one as stated in Eqs. 8 and 12–14 namely

$$\frac{\partial U_i^{(2)}}{\partial x_i} = 0 \tag{34}$$

$$U_0 \frac{\partial U_i^{(2)}}{\partial x} + W^{(2)} \frac{dU_0}{dz} \delta_{i1} = -\frac{\partial P^{(2)}}{\partial x_i} - \frac{2}{3} \frac{\partial k^{(2)}}{\partial x_i} + (v_{t0} + \nu) \frac{\partial^2 U_i^{(2)}}{\partial x_j^2} + \frac{dv_{t0}}{dz} \left(\frac{\partial U_i^{(2)}}{\partial z} + \frac{\partial W^{(2)}}{\partial x_i} \right) + \frac{\partial}{\partial z} \left(v_t^{(2)} \frac{dU_0}{dz} \right) \delta_{i1} + \frac{\partial v_t^{(2)}}{\partial x} \frac{dU_0}{dz} \delta_{i3} + N_{U_i}^{(2)} + S_{U_i}^{(2)}, \tag{35}$$

$$v_{t2} = \psi_k k^{(2)} + \psi_\epsilon \epsilon^{(2)}, \tag{36}$$

$$U_0 \frac{\partial k^{(2)}}{\partial x} + W^{(2)} \frac{dk_0}{dz} = \frac{1}{\sigma_k} \left[(v_{t0} + \nu) \frac{\partial^2 k^{(2)}}{\partial x_j^2} + \frac{dv_{t0}}{dz} \frac{\partial k^{(2)}}{\partial z} + \frac{\partial}{\partial z} \left(v_t^{(2)} \frac{\partial k_0}{\partial z} \right) \right] + \mathcal{P}_{k2} + N_k^{(2)} + S_k^{(2)}, \tag{37}$$

$$U_0 \frac{\partial \epsilon^{(2)}}{\partial x} + W^{(2)} \frac{d\epsilon_0}{dz} = \frac{1}{\sigma_\epsilon} \left[(v_{t0} + \nu \sigma_\epsilon) \frac{\partial^2 \epsilon^{(2)}}{\partial x_j^2} + \frac{dv_{t0}}{dz} \frac{\partial \epsilon^{(2)}}{\partial z} + \frac{\partial}{\partial z} \left(v_t^{(2)} \frac{\partial \epsilon_0}{\partial z} \right) \right] + \mathcal{P}_{\epsilon 2} + N_\epsilon^{(2)} + S_\epsilon^{(2)}, \tag{38}$$

$$\mathcal{P}_{k2} = 2\nu_{t0} \frac{dU_0}{dz} \left(\frac{\partial U^{(2)}}{\partial z} + \frac{\partial W^{(2)}}{\partial x} \right) + \psi_k \left(\frac{dU_0}{dz} \right)^2 k^{(2)} + \psi_\epsilon \left(\frac{dU_0}{dz} \right)^2 \epsilon^{(2)} - \epsilon^{(2)}, \tag{39}$$

$$\mathcal{P}_{\epsilon 2} = C_{\epsilon 1} C_\mu \frac{dU_0}{dz} \left[2k_0 \left(\frac{\partial U^{(2)}}{\partial z} + \frac{\partial W^{(2)}}{\partial x} \right) + \frac{dU_0}{dz} k^{(2)} \right] + C_{\epsilon 2} \frac{\epsilon_0}{k_0} \left(\frac{\epsilon_0}{k_0} k^{(2)} - 2\epsilon^{(2)} \right). \tag{40}$$

The only difference existing between the first- and second-order correction lies in the forcing terms that are

$$S_U^{(2)} = -c_d a_f \left[\left| \mathbf{U}_0 + \mathbf{U}^{(1)} + \mathbf{U}^{(2)} \right| \left(\mathbf{U}_0 + \mathbf{U}^{(1)} + \mathbf{U}^{(2)} \right) - \left| \mathbf{U}_0 + \mathbf{U}^{(1)} \right| \left(\mathbf{U}_0 + \mathbf{U}^{(1)} \right) \right] - \lambda(x) \mathbf{U}^{(2)}, \tag{41}$$

$$S_k^{(2)} = -\beta_p c_d a_f \left[\left| \mathbf{U}_0 + \mathbf{U}^{(1)} + \mathbf{U}^{(2)} \right| \left(k_0 + k^{(1)} + k^{(2)} \right) - \left| \mathbf{U}_0 + \mathbf{U}^{(1)} \right| \left(k_0 + k^{(1)} \right) \right] - \lambda(x) k^{(2)}, \tag{42}$$

$$S_\epsilon^{(2)} = -\beta_p C_{\epsilon 5} c_d a_f \left[\left| \mathbf{U}_0 + \mathbf{U}^{(1)} + \mathbf{U}^{(2)} \right| \left(\epsilon_0 + \epsilon^{(1)} + \epsilon^{(2)} \right) - \left| \mathbf{U}_0 + \mathbf{U}^{(1)} \right| \left(\epsilon_0 + \epsilon^{(1)} \right) \right] - \lambda(x) \epsilon^{(2)}, \tag{43}$$

$$N_{U_i}^{(2)} = -U_j^{(1)} \frac{\partial U_i^{(1)}}{\partial x_j} + \frac{\partial}{\partial x_j} \left[v_t^{(1)} \left(\frac{\partial U_i^{(1)}}{\partial x_j} + \frac{\partial U_j^{(1)}}{\partial x_i} \right) + \omega \frac{dU_0}{dz} \left(\delta_{i1} \delta_{j3} + \delta_{i3} \delta_{j1} \right) \right], \tag{44}$$

$$N_k^{(2)} = -U_j^{(1)} \frac{\partial k^{(1)}}{\partial x_j} + \frac{\partial}{\partial x_j} \left[v_t^{(1)} \frac{\partial k^{(1)}}{\partial x_j} + \omega \frac{dk_0}{dz} \right] + \nu_{t0} \frac{\partial U_i^{(1)}}{\partial x_j} \left(\frac{\partial U_i^{(1)}}{\partial x_j} + \frac{\partial U_j^{(1)}}{\partial x_i} \right) + 2\nu_t^{(1)} \frac{dU_0}{dz} \left(\frac{\partial U^{(1)}}{\partial z} + \frac{\partial W^{(1)}}{\partial x} \right) + \omega \left(\frac{dU_0}{dz} \right)^2, \tag{45}$$

$$N_\epsilon^{(2)} = -U_j^{(1)} \frac{\partial \epsilon^{(1)}}{\partial x_j} + \frac{1}{\sigma_\epsilon} \frac{\partial}{\partial x_j} \left[v_t^{(1)} \frac{\partial \epsilon^{(1)}}{\partial x_j} + \omega \frac{d\epsilon_0}{dz} \right] + C_{\epsilon 1} C_\mu \left[k_0 \frac{\partial U_i^{(1)}}{\partial x_j} \left(\frac{\partial U_i^{(1)}}{\partial x_j} + \frac{\partial U_j^{(1)}}{\partial x_i} \right) + 2k^{(1)} \frac{dU_0}{dz} \left(\frac{\partial U^{(1)}}{\partial z} + \frac{\partial W^{(1)}}{\partial x} \right) \right] - C_{\epsilon 2} \frac{\epsilon_0^2}{k_0} \left[\left(\frac{k^{(1)}}{k_0} \right)^2 + \left(\frac{\epsilon^{(1)}}{\epsilon_0} \right)^2 - 2 \frac{k^{(1)} \epsilon^{(1)}}{k_0 \epsilon_0} \right]. \tag{46}$$

$$\omega = C_\mu \frac{(k^{(1)})^2}{\epsilon} + \nu_{t0} \left(\frac{\epsilon^{(1)}}{\epsilon_0} \right)^2 - \psi_k \frac{k^{(1)} \epsilon^{(1)}}{\epsilon_0}. \tag{47}$$

The S terms represent indeed the body forces applied to the flow by both the forest and the fringe region. As evident from Eqs. 41–43, they compensate for the different drag between the first- and the second-order corrections, while the fringe force acts linearly. This methodology is the fastest since it necessities only of an additional linear simulation, rather than an iterative scheme where the first-order correction is allowed to vary as a consequence of the second-order one. On the other hand, the additional body forces 44–46 are due to the non-linear interaction of the first-order field, and they should indeed compensate for the non-linear departure from the first-order correction.

References

- Arnqvist J, Segalini A, Dellwik E, Bergström H (2015) Wind statistics from a forested landscape. *Boundary-Layer Meteorol* 156:53–71
- Baldocchi D, Hutchison B (1988) Turbulence in an almond orchard: spatial variations in spectra and coherence. *Boundary-Layer Meteorol* 42:293–311
- Belcher SE, Jerram N, Hunt JCR (2003) Adjustment of a turbulent boundary layer to a canopy of roughness elements. *J Fluid Mech* 488:369–398
- Chevalier M, Schlatter P, Lundbladh A, Henningson DS (2007) Simson simson. a pseudo-spectral solver for incompressible boundary layer flows. Technical Report TRITA-MEK 2007:07, KTH Mechanics
- Dupont S, Brunet Y (2009) Coherent structures in canopy edge flow: a large-eddy simulation study. *J Fluid Mech* 630:93–128
- Finnigan JJ (2000) Turbulence in plant canopies. *Annu Rev Fluid Mech* 32:519–571
- Garratt JR (1990) The internal boundary layer—a review. *Boundary-Layer Meteorol* 50:171–203
- Hanjalic K (2005) Will RANS survive LES? A view of perspectives. *J Fluids Eng* 127:831–839
- Harman IN, Finnigan JJ (2007) A simple unified theory for flow in the canopy and roughness sublayer. *Boundary-Layer Meteorol* 123:339–363
- Irvine MR, Gardner BA, Hill MK (1997) The evolution of turbulence across a forest edge. *Boundary-Layer Meteorol* 84:467–496
- Jewkes JW, Chung YM, Carpenter PW (2011) Modifications to a turbulent inflow generation method for boundary-layer flows. *AIAA J* 49(1):247–250
- Kametani Y, Fukagata K (2011) Direct numerical simulation of spatially developing turbulent boundary layers with uniform blowing or suction. *J Fluid Mech* 681:154–172
- Katul G, Mahr L, Poggi D, Sanz C (2004) One- and two-equation models for canopy turbulence. *Boundary-Layer Meteorol* 113:81–109
- Kobayashi H (2005) The subgrid-scale models based on coherent structures for rotating homogeneous turbulence and turbulent channel flow. *Phys Fluids* 17(4):045,104
- Lund TS, Wu X, Squires KD (1998) Generation of turbulent inflow data for spatially-developing boundary layer simulations. *J Comput Phys* 140(2):233–258
- Mellor GL, Yamada T (1982) Development of a turbulence closure model for geophysical fluid problems. *Rev Geophys* 20(4):851–875
- Miyauchi T, Tanahashi M, Suzuki M (1994) Inflow and outflow boundary conditions for direct numerical simulations. *Trans J Soc Mech Eng Ser B* 60(571):813–821
- Schlatter P, Örlü R (2010) Assessment of direct numerical simulation data of turbulent boundary layers. *J Fluid Mech* 659:116–126
- Schmid PJ, Henningson DS (2001) *Stability and transition in shear flows*. Springer, Netherlands, 558 pp
- Segalini A, Fransson JHM, Alfredsson PH (2013) Scaling laws in canopy flows: a wind-tunnel analysis. *Boundary-Layer Meteorol* 148:269–283
- Shen J, Tang T, Wang L (2011) *Spectral methods. Algorithms, analysis and applications*. Springer, Netherlands, 472 pp
- Silva Lopes A, Palma JMLM, Viana Lopes J (2013) Improving a two-equation turbulence model for canopy flows using large-eddy simulation. *Boundary-Layer Meteorol* 149:231–257
- Sogachev A, Kelly M (2015) On displacement height, from classical to practical formulation: Stress, turbulent transport and vorticity considerations. *Boundary-Layer Meteorol*. doi:10.1007/s10,546-015-0093-x
- Stacey GR, Belcher RE, Wood CJ, Gardiner BA (1994) Wind flows and forces in a model spruce forest. *Boundary-Layer Meteorol* 69:311–334
- Svensson U, Häggkvist K (1990) A two-equation turbulence model for canopy flows. *J Wind Eng Ind Aerodyn* 35:201–211
- Yang B, Raupach MR, Shaw RH, Paw UKT, Morse AP (2006) Large-eddy simulation of turbulent flow across a forest edge. Part I: flow statistics. *Boundary-Layer Meteorol* 120:377–412
- Zilitinkevich S, Elperin T, Kleorin N, Rogachevskii I, Esau I (2013) A hierarchy of energy- and flux-budget (EFB) turbulence closure models for stably-stratified geophysical flows. *Boundary-Layer Meteorol* 146:341–373